



Insight into the excellent catalytic activity of (CoMo)S₂/graphene for hydrogen evolution reaction

Li Xin Chen¹, Zhi Wen Chen¹, Ying Zhang, Chun Cheng Yang*, Qing Jiang*

Key Laboratory of Automobile Materials (Jilin University), Ministry of Education, and School of Materials Science and Engineering, Jilin University, Changchun, 130022, China

ARTICLE INFO

Keywords:

Hydrogen evolution reaction
Catalysts design
Density functional theory simulations
MoS₂
Graphene

ABSTRACT

Electrochemical water splitting has become a potential pathway for sustainable hydrogen production, where high-efficiency low-cost catalysts are highly desirable. MoS₂ is a promising candidate to substitute effective but expensive Pt-based catalysts for hydrogen evolution reaction. In this work, the computer simulation results reveal that alloying with Co and compositing with graphene could significantly improve the electrocatalytic performance of MoS₂ thanks to the activation of MoS₂ inert surfaces and enhanced electron transport. Based on this finding, we designed and synthesized a catalyst of (CoMo)S₂/graphene, which exhibits excellent performance with low onset potential (28 mV), overpotential (100 mV) for driving a current density of 10 mA cm⁻², and Tafel slope (60.8 mV dec⁻¹), superior to most of MoS₂-based electrocatalysts reported in open literatures. This study supplies important information for fundamental understanding of high-efficiency non-noble electrocatalysts toward applications in energy-conversion devices.

1. Introduction

Energy crisis and climate change derived from fossil fuel combustion have become major concerns. The exploitation of clean and renewable energy sources is thus imperative. H₂ has gained increased interests because of the highest energy density of 142 MJ kg⁻¹ [1–3]. The electrochemical water splitting is an economical and effective approach to produce H₂ [4,5], where highly active catalysts are needed in order to achieve low overpotentials and fast kinetics [6–8]. The current hydrogen evolution reaction (HER) electrocatalysts are Pt and Pt-based materials, which are scarce and expensive, severely limiting their applications [9–11]. Thus, it is highly desirable to explore non-noble HER electrocatalysts with high efficiency [12–15].

MoS₂, as a two-dimensional (2D) material with intriguing physical and chemical properties, has gained tremendous attentions for HER during the past few years [16–22]. In general, the active centers of MoS₂ are considered as coordinatively unsaturated edge sites due to their appropriate hydrogen adsorption free energy, while the in-plane domains of MoS₂ are inert [23,24]. To further boost the HER activity of MoS₂, two strategies were frequently utilized through increasing exposed edges and improving intrinsic activity of active sites per unit area [25,26]. On the basis of these two strategies, various approaches have been proposed. Chatti et al. prepared a composite of vertically-oriented

MoS₂ nanosheets on graphene support by using microwave synthesis, which shows outstanding electrocatalytic performance due to high-concentration edge sites and improved electrical conductivity [15]. Jaramillo et al. enhanced the catalytic activity of MoS₂ via preferentially exposed edges [27]. Ye et al. introduced numerous edge sites through O₂ plasma and H₂ treatments on monolayer MoS₂, leading to high catalytic activity [28]. Yang et al. fabricated edge-oriented MoS₂ film with more active sites, delivering superb catalytic performance [29]. Compared with edge sites, the activated inert basal planes of MoS₂ showed greater potential for catalyzing HER through single metal atom doping, or surface S-vacancy formation [16,30–32].

Recently, Bao's group introduced single-atom Pt into the basal plane of MoS₂ nanosheets (Pt-MoS₂) [16]. A significant improvement of HER activity on Pt-MoS₂ with high stability was achieved in the acidic medium. Moreover, the in-plane domains of monolayer MoS₂ were also activated via creating S vacancies [30]. The corresponding catalytic performance could be regulated by adjusting strain and vacancy concentration. However, the doping of noble Pt and complex preparation process of S vacancies increase the electrocatalysts cost, thus limiting their applications. Moreover, the low defect concentrations from noble metal doping and S-vacancy creating impeded HER activity of MoS₂ [16,30]. On the contrary, alloying with non-noble Co into MoS₂ is an economical method to activate abundant inert surfaces [33]. It has also

* Corresponding authors.

E-mail addresses: ccyang@jlu.edu.cn (C.C. Yang), jiangq@jlu.edu.cn (Q. Jiang).

¹ These authors contributed equally to this work.

been demonstrated that non-noble metals (e.g., Co, Ni) doping could improve the catalytic activity of MoS₂ via adjusting its electronic structure [24,34].

Based on the aforementioned considerations, our strategy strives to activate in-plane domains of MoS₂ through Co alloying to form (CoMo)S₂. Moreover, our recent work has demonstrated that reduced graphite oxide (RGO) is beneficial for high electrical conductivity and suitable hydrogen adsorption free energy [35]. Thus, in this work, we designed a hybrid HER catalyst of (CoMo)S₂/RGO under the guidance of density functional theory (DFT) simulations. As expected, the composite shows an outstanding catalytic performance with the onset potential of 28 mV and a small overpotential of 100 mV at a current density of 10 mA cm⁻² because of the synergistic effects between (CoMo)S₂ and RGO. The low cost and outstanding catalytic performance make (CoMo)S₂/RGO a potential candidate to replace Pt-based catalysts toward HER.

2. Catalyst design aided by DFT simulations

2.1. Simulation method

In this work, the spin-polarized DFT in the DMol³ code is used for the catalyst design [36,37]. A generalized gradient approximation (GGA) with Perdew-Burke-Ernzerhof (PBE) describes exchange-correlation effects [38]. The relativistic effect is considered by a DFT semi-core pseudo potentials (DSPPs) core treatment [39]. This means that core electrons are described by a single effective potential. Moreover, the basis set is double numerical plus polarization (DNP) with fine quality for the orbital cutoff. The geometrically optimized structures are obtained until the maximum displacement, maximum energy gradient, and energy change become less than 5.0×10^{-3} Å, 2.0×10^{-3} Ha/Å, and 1.0×10^{-5} Ha, respectively. The corresponding k-point sampling of the Brillouin zone and the smearing parameter are set as $4 \times 4 \times 1$ grid and 5.0×10^{-3} Ha, respectively.

The computational hydrogen electrode (CHE) model is used for calculating free energies [40]. The adsorption free energy of hydrogen (ΔG_{H^*}) is given by $\Delta G_{H^*} = \Delta E_{H^*} + \Delta ZPE - T\Delta S + \Delta G_U$, where ΔE_{H^*} , ΔZPE , T , ΔS and ΔG_U are the adsorption energy of hydrogen, zero point energy, absolute temperature, entropy change, and free energy contribution from the electrode potential (U), respectively. Furthermore, ΔE_{H^*} is determined by $\Delta E_{H^*} = E_{H^*} - E_{cat} - E_H$, where E_{H^*} , E_{cat} and E_H are total energies of the adsorbed system, the isolate system, and 1/2 H₂ (gas), respectively.

2.2. DFT-aided catalyst design

The conductivity of electrocatalysts plays a vital role for HER, which requires fast electron transfer in the catalytic processes [30,41]. Unfortunately, the pristine monolayer MoS₂ owns a large direct band gap of 1.80 eV [42], indicating poor electrical conductivity. To conquer this drawback, two strategies were used: (1) alloying with Co to form the impurity levels; and (2) compositing with a conductive graphene.

Firstly, we vindicate the accuracy of our simulation method by calculating the band gap of the pristine monolayer MoS₂, which is 1.74 eV at K-point (see Fig. 1a and b), consisting with the reported value of 1.80 eV [42]. Fig. 1c and d displays the geometric optimization structure and band structure of (CoMo)S₂, respectively. After alloying with Co, the Fermi level of (CoMo)S₂ moves up 1.20 eV in comparison to that of pristine monolayer MoS₂, implying n-type doping of MoS₂. A large number of electrons transfer from Co to adjacent S of MoS₂ and the band gap decreases from 1.74 eV of MoS₂ to 0.28 eV of (CoMo)S₂ due to the formation of impurity levels (see Fig. 1d), which is beneficial for electrocatalysis [34]. To further increase the electronic conductivity, graphene is introduced to form the (CoMo)S₂/graphene heterointerface and the corresponding geometric optimization structure and band structure are shown in Fig. 1e and f, respectively. It can be found that (CoMo)S₂/graphene endows a similar conductive behavior

to graphene. In addition, the Fermi level shifts down 0.20 eV compared with that of (CoMo)S₂ due to the electron transfer from (CoMo)S₂ to graphene. The binding energies of MoS₂/graphene and (CoMo)S₂/graphene calculated are -2.23 and -2.30 eV, respectively, which indicate that the heterointerface structure becomes more stable after Co alloying.

Furthermore, the hydrogen adsorption free energy ΔG_{H^*} was calculated to evaluate the HER performance. As shown in Fig. 1g, the HER pathway can be depicted through an initial state of H⁺ + e⁻, an intermediate state of adsorbed H (H*), and a final state of 1/2 the H₂ product [43]. In the volcano plot of HER, the ΔG_{H^*} value on the volcanic vent is about 0 eV, indicating the optimal HER activity [23]. The inert plane of MoS₂ owns a ΔG_{H^*} value of 1.93 eV, which implies an energetically unfavourable adsorption process of hydrogen, resulting in a sluggish Volmer reaction. As shown in Fig. 1c, the inert S (site "1") is activated by the nearest neighbor Co due to the electron transfer from Co to S. The calculated ΔG_{H^*} is -0.18 eV, implying an appreciable HER activity. The corresponding adsorption structure is shown in Fig. S1. More intriguing is that the (CoMo)S₂/graphene endows a near zero ΔG_{H^*} of -0.12 eV, which is much closer to that of Pt (ΔG_{H^*} = -0.09 eV). Moreover, the ΔG_{H^*} values of other sites (sites "2", "3" and "4" in Fig. 1c and e) were also calculated and listed in Table S1. Only the site "2" has a catalytic activity for HER while other sites are inert. As a result, the (CoMo)S₂/graphene should possess excellent HER performance with high electrical conductivity and appropriate ΔG_{H^*} value through rational design based on DFT simulations.

3. Experimental section

3.1. Materials

Cobalt dichloride (CoCl₂·6H₂O) and ammonia water (NH₃·H₂O) were bought from Sinopharm Chemical Reagent Co., Ltd. Ammonium tetrathiomolybdate [(NH₄)₂MoS₄], hydrazine hydrate (N₂H₄·H₂O) and graphite flake were bought from Sigma Aldrich. The above chemicals are of analytical purity and applied directly.

3.2. Catalyst preparation

Graphene oxide (GO) was synthesized according to a modified Hummers' method [44], which was described in detail elsewhere [45]. 0.48 ml GO (roughly corresponding to a molar ratio of MoS₂/RGO = 5) was then dispersed in ultrapure water to form the dispersion liquid (0.5 mg ml⁻¹). For the synthesis of (CoMo)S₂ precursor, 1 mmol (NH₄)₂MoS₄ and 1 mmol CoCl₂·6H₂O were dispersed in 20 ml ultrapure water, respectively. Then, the CoCl₂ solution was added into the (NH₄)₂MoS₄ solution drop by drop under stirring for 30 min. Subsequently, the (CoMo)S₂ precursor were incorporated with the GO dispersion. After sonicating for 30 min, 4.72 μl N₂H₄·H₂O and 75.6 μl NH₃·H₂O were added into the mixture. Then, the mixture was put into an oil bath (95 °C) for 1 h, reducing GO into RGO. The resulting suspension was filtered, washed and dried at 60 °C overnight. After that, the fabricated composite was annealed at 500 °C for 5 h under N₂ atmosphere. The final product was treated with HCl (3 M), washed by using ultrapure water and ethanol, and dried at 60 °C. For comparison, (CoMo)S₂ was prepared under the same process without the co-reduction treatment of GO. Moreover, to optimize the RGO content in (CoMo)S₂/RGO, two other samples were prepared using 0.24 ml and 2.40 ml GO (roughly corresponding to molar ratios of MoS₂/RGO = 10 and = 1, respectively) as the precursor in this work.

3.3. Catalyst characterization

X-ray diffraction (XRD) was performed on a D/max2500 pc diffractometer with Cu Kα radiation (λ = 0.15406 nm). Field-emission scanning electron microscope (FESEM, JSM-6700 F, JEOL, 15 keV) and

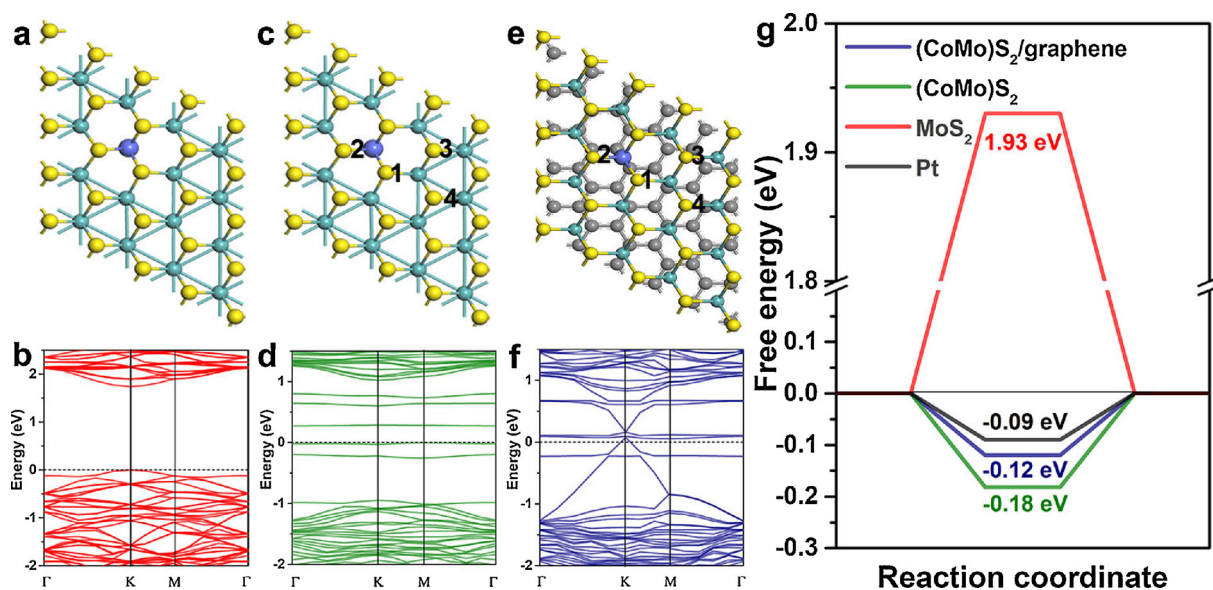


Fig. 1. DFT simulation results. The geometrically optimized structures and band structures of MoS₂ [(a) and (b)], (CoMo)S₂ [(c) and (d)] and (CoMo)S₂/graphene [(e) and (f)]; (g) describes the free energy diagram of hydrogen evolution at “standard” conditions corresponding to 1 bar of H₂ and pH = 0 at 300 K. The yellow, azure, cyan and grey balls represent S, Mo, Co and C atoms. The numbers in (c) and (e) denote various adsorption sites of H atom. The dotted lines in (b), (d), and (f) indicate the Fermi level. (For interpretation of the references to colour in this figure legend, the reader is referred to the web version of this article).

transmission electron microscope (TEM, JEM-2100 F, JEOL, 200 keV) were used to characterize samples' surface morphology and micro-structure. X-ray photoelectron spectroscopy (XPS) was carried on an ESCALAB 250 spectrometer with a monochromatic Al-K_α (1486.6 eV) source. Raman spectrum was recorded on a micro-Raman spectrometer (Renishaw) using a laser source with 532-nm excitation wavelength. The nitrogen adsorption and desorption measurements were performed on a Micromeritics ASAP 2020 analyzer to determine the specific area and pore size distribution of samples.

3.4. Electrochemical measurements

Electrochemical measurements were performed on an Ivium-n-Stat electrochemical workstation in a standard three-electrode system at room temperature. The working electrode is a glassy carbon rotating disk electrode (RDE, Pine Research Instrumentation) with a diameter of 5 mm, which is covered by a thin catalyst film. A graphite rod and a saturated calomel electrode (Hg/Hg₂Cl₂, SCE) are used as the counter electrode and reference electrode, respectively. Typically, catalyst ink was prepared as follows. 3 mg catalyst powders were dispersed in 0.5 ml mixture of water-isopropanol solution (4:1, v/v) and 50 μ l 5 wt% Nafion solution. After that, the above mixture was sonicated for 30 min to generate a uniform ink. Then, 30 μ l as-obtained catalyst ink was pipetted using a micro-pipettor and loaded onto the freshly polished glassy carbon electrode (GCE). After naturally drying at room temperature, the catalyst film was finally obtained. Similar preparation methods have been reported in open literatures [9,15,33]. Here, isopropanol can disperse the solid mixture, which is beneficial for the formation of uniform film to cover the whole GCE after the drying of the catalyst ink. Nafion was used as a reinforcing layer for robust films adhered to the electrode surface, resulting in a superior durability of the electrode during electrochemical measurements [46]. Linear sweep voltammetry (LSV) measurement was conducted on RDE in 0.5 M sulfuric acid (H₂SO₄) at a rotation rate of 2025 rpm and a scan rate of 5 mV s⁻¹. Note that the disk electrode's planner surface with the catalyst has direct contact with the electrolyte solution. When the electrode is rotating, the solution runs from the bulk to the electrode surface, and then flows away along the direction parallel to the disk surface [47]. Electrochemical impedance spectroscopy (EIS) was performed at an

overpotential (η) of 0.15 V (vs. RHE) from 100 K Hz to 0.1 Hz [33]. Stability tests were conducted using continuous cyclic voltammetry (CV) from -0.15 to 0.1 V (vs. RHE) with a sweep rate of 100 mV s⁻¹. The time dependence of the current density is measured at a static overpotential of -0.08 V (vs. RHE) for 20000 s. All potential data were calibrated with respect to the RHE via $E(\text{RHE}) = E(\text{SCE}) + 0.273 \text{ V}$. Note that the electrolyte solution was purified with N₂ for 30 min to remove oxygen completely before electrochemical tests. The hydrogen production efficiency experiments were conducted in 0.5 M H₂SO₄ at a potential of -0.3 V (vs. RHE) for 220 min. Thereinto, Ar gas was delivered into the electrolyte with a rate of 30 ml/min (at ambient pressure and room temperature) and routed directly into the gas sampling loop of a gas chromatograph (GC-2014). The composition analysis of gas phase products was performed every 20 min using GC. The gas sample was routed through a packed MoleSieve 5A column and a packed Rt-Q-BOND column before passing a pulsed discharge detector for H₂ quantification. Moreover, helium was used as a carrier.

4. Results and discussion

Based on the DFT-aided catalyst design, a (CoMo)S₂/RGO composite was fabricated by chemical synthesis, annealing and acid treatment, which is schematically shown in Fig. 2. As comparative samples, bare MoS₂ and (CoMo)S₂ were also fabricated. To study the influence of different RGO contents on the catalytic activity of (CoMo)S₂/RGO for HER, three samples were synthesized using different amounts of GO (0.24, 0.48, and 2.40 ml). It is found that 0.48 ml is the optimal amount, which will be discussed below. Thus, the aftermentioned (CoMo)S₂/RGO composite denotes the sample fabricated by adding 0.48 ml GO unless otherwise specified.

Fig. 3 shows the microstructure and morphology characterizations of the (CoMo)S₂/RGO composite. From the XRD patterns (see Fig. 3a), the diffraction peak at around 26.4° for (CoMo)S₂/RGO can be indexed to RGO with graphitic structure, while it is absent for (CoMo)S₂. All rest diffraction peaks correspond well to CoMoS_{3.13} (PDF Card No. 16-0439) [48], indicating that (CoMo)S₂ maintains the layered structure of MoS₂ after Co alloying. Note that some S atoms are missing due to alloying with low-valent Co during the preparation process. Moreover, the (002) peak (at around 14.2°) intensity of (CoMo)S₂/RGO is weaker than that

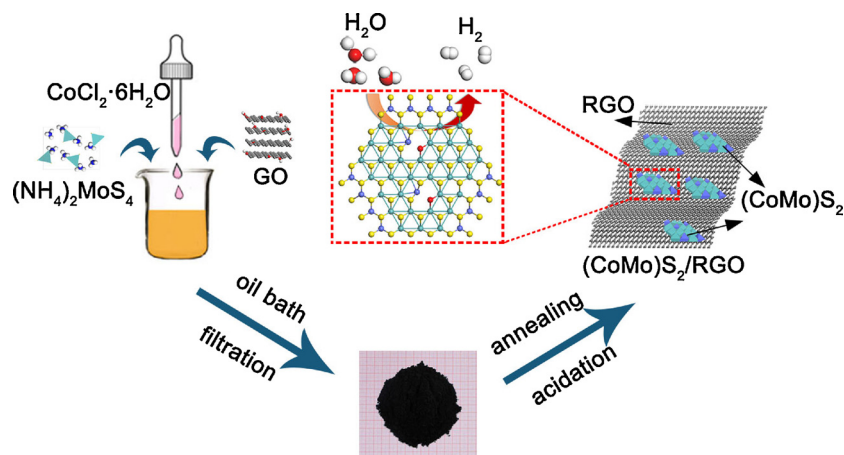


Fig. 2. Schematic illustration for the synthetic route of the (CoMo)S₂/RGO composite.

of (CoMo)S₂, suggesting the prevention of the (CoMo)S₂ stacking via introducing RGO. This would provide more active sites for HER [31]. The structure of (CoMo)S₂/RGO was further investigated by the Raman spectroscopy. As shown in Fig. 3b, the two dominant peaks at 377 and 402 cm⁻¹ are ascribed to the E_{2g}¹ and A_{1g} modes of MoS₂, respectively. The A_{1g} mode shows much higher intensity than that of the E_{2g}¹ mode, indicating edge-terminated structure of (CoMo)S₂/RGO. Such a

structure is beneficial for the HER catalytic activity [33,49,50]. Moreover, RGO is also found in the Raman spectrum (typical D band at 1359 cm⁻¹ and G band at 1581 cm⁻¹, respectively), which is consistent with the XRD pattern. The high intensity ratio of I_D/I_G (~1.29) indicates a large amount of defects and disorders in RGO [42,51,52]. As a result, there are strong interactions between (CoMo)S₂ and RGO, which not only improve the stability of (CoMo)S₂/RGO but also accelerate

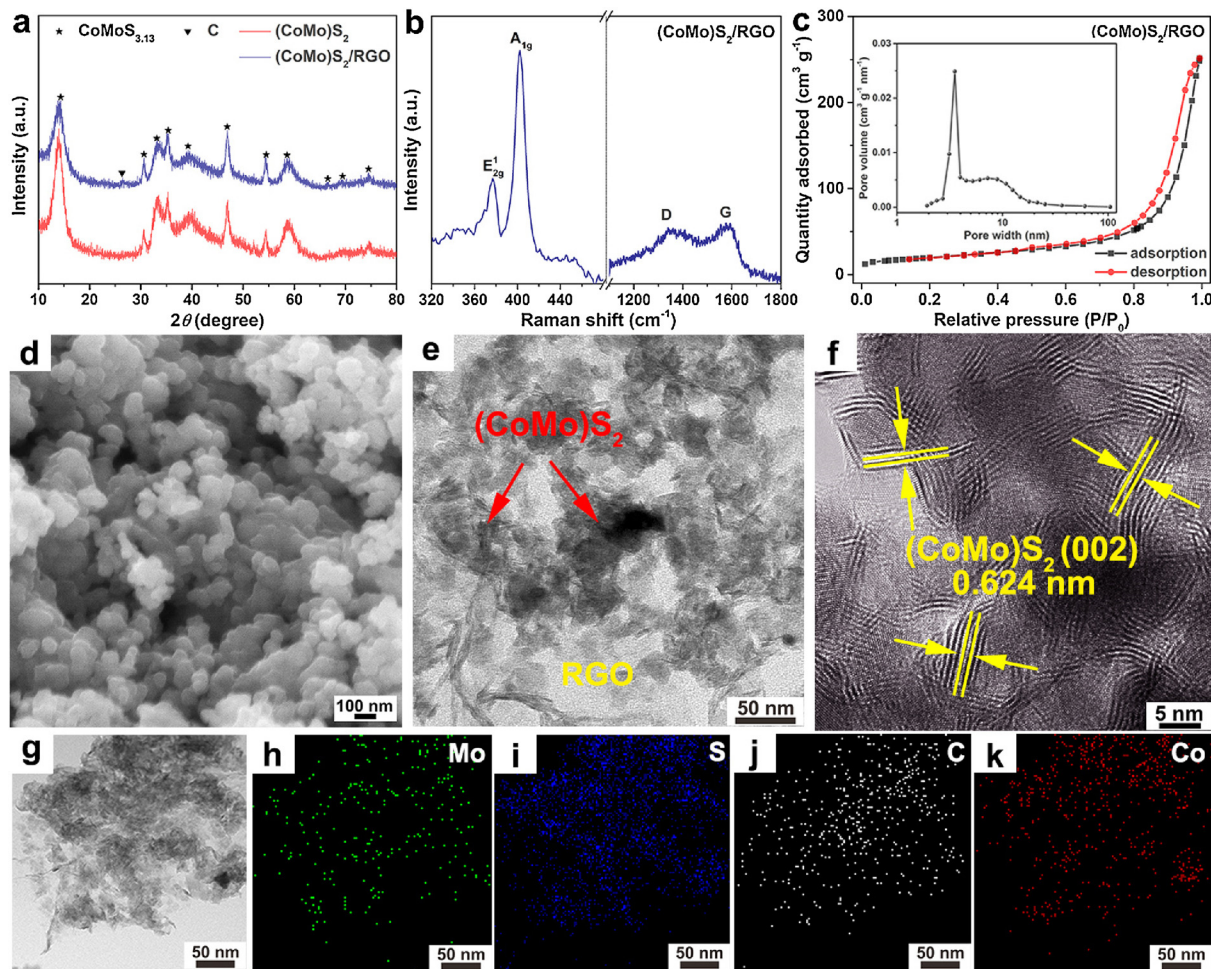


Fig. 3. Microstructure and morphology characterizations. (a) XRD patterns of (CoMo)S₂ and (CoMo)S₂/RGO; (b) Raman spectrum and (c) N₂ adsorption/desorption isotherms and pore size distribution (the inset) of (CoMo)S₂/RGO; (d–f) SEM, TEM and HRTEM images of (CoMo)S₂/RGO; (g–k) scanning TEM image and the corresponding EDX mappings of (CoMo)S₂/RGO.

electron transport in HER. Fig. 3c presents N_2 adsorption/desorption isotherms of $(CoMo)S_2/RGO$. The specific surface area measured is $69.9\text{ m}^2\text{ g}^{-1}$ based on the Brunauer-Emmer-Teller (BET) model. From the inset of Fig. 3c, the pore size is about 3.25 nm according to the Barrett-Joyner-Halenda (BJH) method. The large specific surface area and broad mesopore size distribution originate from the disorder assembly of MoS_2 nanoflakes and graphene sheets with different sizes [53], which could provide more active sites for HER and accelerate the H^+ and H_2 diffusion during the HER process.

Fig. 3d shows an SEM image of $(CoMo)S_2/RGO$, where the $(CoMo)S_2$ nanoparticles (average diameter of $\sim 70\text{ nm}$) are formed by stacking $(CoMo)S_2$ nanosheets. On the contrary, the aggregation is observed (see Fig. S2) for bare $(CoMo)S_2$ synthesized by the same experimental process without RGO owing to high surface energy. This suggests that the presence of RGO in the composite can inhibit the agglomeration of $(CoMo)S_2$ nanoparticles [42]. Fig. 3e presents a TEM image of $(CoMo)S_2/RGO$, where the $(CoMo)S_2$ nanoparticles are uniformly distributed on RGO due to the interaction between $(CoMo)S_2$ and RGO. Thus, more active sites could be exposed for the composite. Also, the introduction of RGO can enhance the electrical conductivity of $(CoMo)S_2/RGO$. Fig. 3f shows an HRTEM image of $(CoMo)S_2/RGO$. The inter-planar spacing of 0.624 nm corresponds to the (002) plane of $(CoMo)S_2$, which indicates that the introduction of Co atoms does not change the layer structure of MoS_2 . The scanning TEM image and energy dispersive X-ray spectrum (EDX) mappings of $(CoMo)S_2/RGO$ are shown in Fig. 3g–k, demonstrating homogeneous distribution of Mo, S, C and Co in $(CoMo)S_2/RGO$. The quantitative element concentration analysis has been performed for $(CoMo)S_2/RGO$ via EDX measurements. The atomic ratio is 3.2:5.4:15.3 for Co:Mo:S. Thus, the ratio of S/(CoMo) is 1.8, very close to the stoichiometric ratio ($= 2$) of $(CoMo)S_2$. The small difference (~ 0.2) may be attributed to influences of some intrinsic factors of EDX, such as fluorescence yields, X-ray adsorption, detector collection angle, detector efficiency etc. [54,55].

The surface electronic states of $(CoMo)S_2/RGO$ were characterized by XPS. From the survey spectrum of $(CoMo)S_2/RGO$ (see Fig. 4a), Mo, S, Co, C and O elements are clearly identified. Fig. 4b–f plots high-resolution XPS spectra of Mo 3d, S 2p, C 1s, Co 2p and O 1s, respectively. As shown in Fig. 4b, six fitted peaks exist in the Mo 3d spectrum,

where the peak located at 226.5 eV can be assigned to S 2s of MoS_2 . The peaks located at 229.2 eV and 232.3 eV are typical characteristic peaks (Mo $3d_{5/2}$ and $3d_{3/2}$, respectively) of MoS_2 , while the relatively higher binding energy peaks of Mo $3d_{5/2}$ (229.5 eV) and Mo $3d_{3/2}$ (232.8 eV) indicate the existence of Mo^{5+} ions. The peak at 235.9 eV can be attributed to MoO_3 , which is possibly generated during the catalyst preparation and exposure to air [56,57]. The sulfur species are identified from S 2p spectrum (see Fig. 4c). The peaks of S $2p_{3/2}$ (162.0 eV) and S $2p_{1/2}$ (163.2 eV) are assigned to the S^{2-} of MoS_2 . Additionally, the S $2p_{3/2}$ (162.7 eV) and $2p_{1/2}$ (164.1 eV) show the presence of bridging S_2^{2-} . The existence of S with a higher binding energy indicates potential HER active sites [58–60]. For C 1s XPS spectrum (see Fig. 4d), the weak peak intensities of C–O and C=O bond demonstrate that the oxygen-containing groups in RGO have been removed successfully [51,61]. The Co 2p spectrum is fitted with four doublets (see Fig. 4e). The first one at 779.2 eV and 794.1 eV are attributed to $2p_{3/2}$ and $2p_{1/2}$ of the $CoMoS$ phase. The second one at 780.5 eV and 796.9 eV are Co^{2+} $2p_{3/2}$ and Co^{2+} $2p_{1/2}$, respectively. The third and fourth belong to the satellite peaks [33,62]. For the O 1s spectrum (see Fig. 4f), the peaks of C–O, C=O and Mo–O bonds are located at 532.4, 531.7, and 529.9 eV, respectively, which indicate that the O atoms come from the residual GO and partial oxidation of the sample during the preparation process.

To investigate the HER performance in an acidic electrolyte (0.5 M H_2SO_4), electrochemical measurements were performed using an RDE apparatus in a standard three-electrode system. Fig. 5a and b shows the LSV and corresponding Tafel plots, respectively. The commercial Pt/C, bulk MoS_2 and $(CoMo)S_2$ were also measured for comparisons. The effects of bare GCE and RGO on the electrochemical performance are negligible due to their little activity for HER (see Fig. S3). As shown in Fig. 5a, the best electrocatalyst Pt/C exhibits the smallest onset potential (0 mV) and the lowest overpotential (38 mV) at a current density of 10 mA cm^{-2} , which is subsequently used as a reference to other catalysts [63,64]. The bulk MoS_2 presents almost no catalytic activity because of its slow electron transport and inert basal plane. The $(CoMo)S_2$ catalyst shows a lower onset potential of 128 mV compared with bulk MoS_2 thanks to the activation of inert planes of MoS_2 by alloying with Co. From Table 1, the $(CoMo)S_2/RGO$ composite exhibits a lower

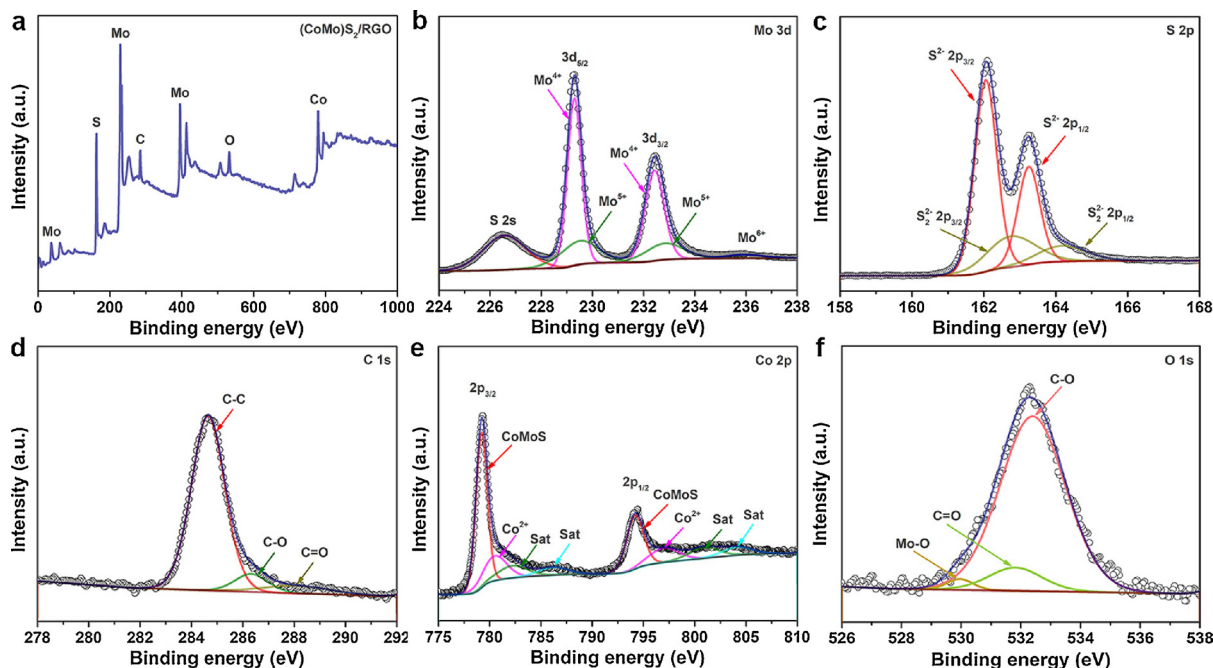


Fig. 4. X-ray photoelectron spectroscopy spectra. (a) XPS survey spectrum of $(CoMo)S_2/RGO$; (b)–(f) High-resolution XPS spectra of Mo 3d, S 2p, C 1s, Co 2p and O 1s of $(CoMo)S_2/RGO$, respectively.

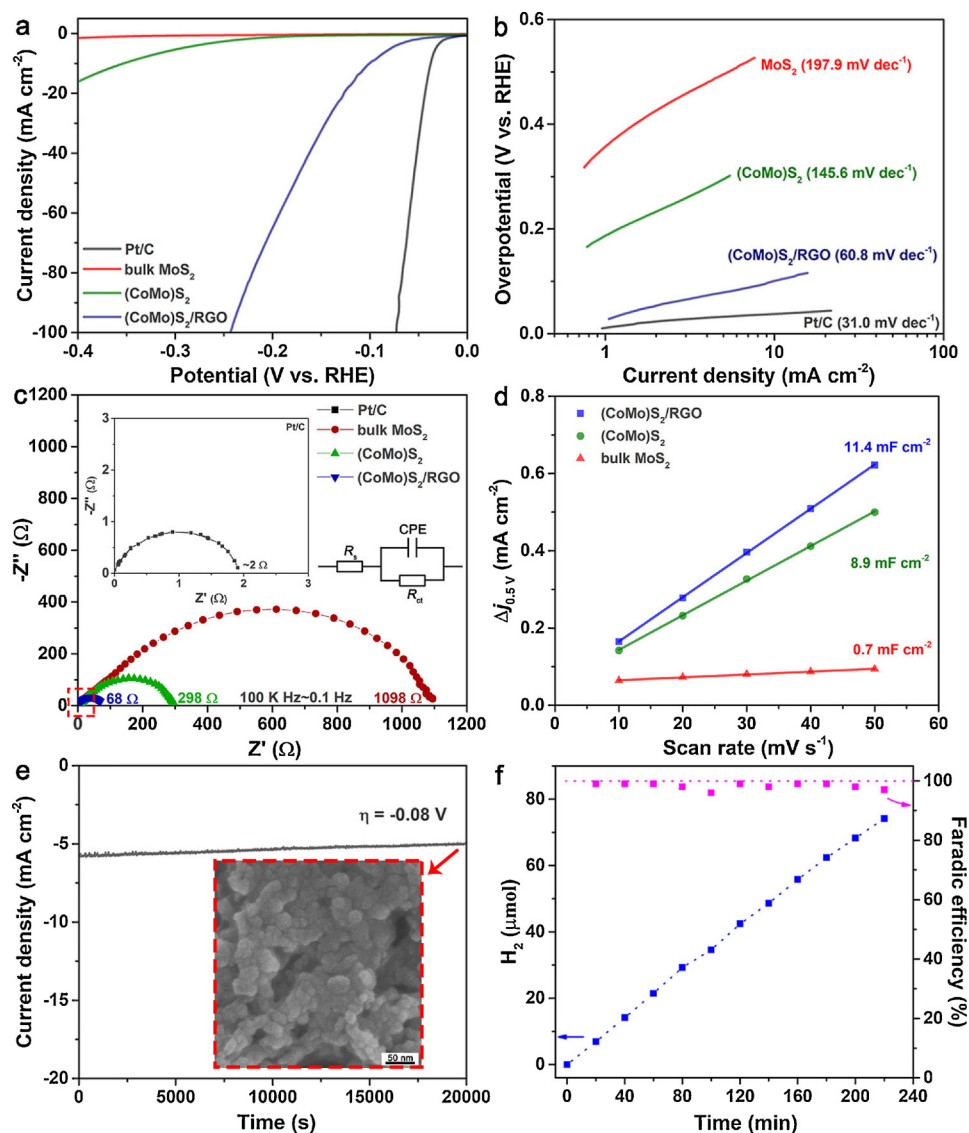


Fig. 5. Electrochemical performances. (a) Polarization curves of Pt/C, bulk MoS₂, (CoMo)S₂ and (CoMo)S₂/RGO; (b) Tafel curves of Pt/C, bulk MoS₂, (CoMo)S₂ and (CoMo)S₂/RGO; (c) Nyquist plots for Pt/C (see the inset for an enlarged plot), bulk MoS₂, (CoMo)S₂ and (CoMo)S₂/RGO [the applied potential is 0.15 V (vs. RHE) from 100 K Hz to 0.1 Hz]; (d) The capacitive currents at 0.5 V as a function of scan rate for bulk MoS₂, (CoMo)S₂ and (CoMo)S₂/RGO; (e) Time-dependent current density curve of (CoMo)S₂/RGO under a static overpotential of -0.08 V vs. RHE for 20000 s [the inset is an SEM image of (CoMo)S₂/RGO after a 20000 s durability test]; (f) The production rate and Faradic efficiency of (CoMo)S₂/RGO for hydrogen generation.

overpotential of 100 mV for driving a current density of 10 mA cm⁻² among MoS₂-based electrocatalysts reported in open literatures apart from P-MoS₂@hierarchical carbon microflower (86 mV) and Pd-MoS₂ (78 mV). Moreover, (CoMo)S₂/RGO possesses the onset potential of 28 mV, which is much lower than those of other electrocatalysts as listed in Table 1 (except for MoS₂/Ti₃C₂-Mxene@C). The composition effect on HER catalytic performance of (CoMo)S₂/RGO was investigated by considering different amounts of the precursor of GO. As shown in Fig. S4, the (CoMo)S₂/RGO hybrid synthesized by adding 0.48 ml GO exhibits the lowest overpotential of 100 mV at 10 mA cm⁻², relative to other two samples (144 mV for 2.40 ml GO and 200 mV for 0.24 ml GO). Thus, 0.48 ml is the optimum adding amount, which ensures a balance between the electrical conductivity and active sites number. Fewer GO could not provide sufficient electrical conductivity while excess GO would cover some active sites of the catalyst.

To further substantiate the elevated HER efficiency of (CoMo)S₂/RGO catalyst, the corresponding Tafel slopes were measured, as shown in Fig. 5b. Pt/C shows a Tafel slope of ~31.0 mV dec⁻¹, which is consistent with the previously reported values. This indicates that our electrochemical measurements data are reliable [16,60]. The Tafel slope of (CoMo)S₂ is 145.6 mV dec⁻¹, which is better than that of bulk MoS₂ (197.9 mV dec⁻¹). Meanwhile, the (CoMo)S₂/RGO displays a much smaller slope (60.8 mV dec⁻¹) compared with (CoMo)S₂ and bulk

MoS₂, demonstrating higher catalytic activity.

The hydrogen evolution mechanism can be elucidated by the Tafel slope. In acidic media, three possible reaction steps are involved in HER process, which are H₃O⁺ + e⁻ → H* + H₂O (Volmer reaction), H* + H₃O⁺ + e⁻ → H₂ + H₂O (Heyrovsky reaction), and H* + H* → H₂ (Tafel reaction). The Tafel slope value of 120, 40, or 30 mV dec⁻¹ indicates that the Volmer, Heyrovsky, or Tafel reaction is the rate-determining step, respectively. Here, the Tafel slope of (CoMo)S₂/RGO catalyst is 60.8 mV dec⁻¹, which indicates a Heyrovsky-dominated Volmer-Heyrovsky mechanism [35]. Note that RGO contributes significantly to the enhanced electrical conductivity and thus high HER catalytic performance of (CoMo)S₂/RGO. EIS tests were carried out to evaluate the electrode kinetics for HER (see Fig. 5c). It is found that the Pt/C electrode has the smallest charge-transfer resistance (~2 Ω) among the samples, indicating the fastest electron transport. The Nyquist plots reveal that (CoMo)S₂/RGO shows a remarkable decrease in charge-transfer resistance (R_{ct}) compared with bulk MoS₂ and (CoMo)S₂. This is caused by the improvement of the electrical conductivity through introducing Co and RGO, consistent with the DFT simulation results as illustrated in Fig. 1.

The electrochemical surface areas of the catalysts were evaluated by the electrochemical double layer capacitances (C_{dl}) using CV measurements. The potential range (0.45–0.55 V vs. RHE) is first

Table 1
Comparisons of HER performances among MoS₂-based electrocatalysts.

Electrocatalyst	Onset potential (mV)	Overpotential (mV) at 10 mA cm ⁻²	Tafel slope (mV dec ⁻¹)	Reference
(CoMo)S ₂ /RGO	28	100	60.8	This work
Ni-Co-MoS ₂	125	155	51	[18]
Co-mesoporous MoS ₂ foam		156	74	[24]
CoMoS ₃ hollow prism	75	171	56.9	[25]
NPNi-MoS ₂ /RGO	85	205	71.3	[35]
MoS ₂ /graphene	30	110	67.4	[51]
MoS ₂ /Ti ₃ C ₂ -Mxene@C	20	135	45	[67]
Porous MoO ₂ /MoS ₂	104	240	76.1	[68]
MoS ₂ -rGO/Mo	100	188	64	[69]
MoS ₂ /multiwalled carbon nanotube	222		62.7	[70]
1T/2H MoS ₂	120	220	61	[71]
MoS ₂ /N-Graphdiyne	88	186	63	[72]
MoS ₂ (1-3)Px		150	57	[73]
MoS ₂ /N-carbon nanotube	75	110	40	[74]
NF-MoS ₂	110		57	[75]
NiS ₂ /MoS ₂		235	58	[76]
MoS ₂ -MoP/C	64	102	58	[77]
Zn-MoS ₂	130		51	[78]
MoS ₂ /Ti ₃ C ₂ T _x	30	152	70	[79]
P-MoS ₂ @hierarchical carbon microflower		86	42	[80]
Pd-MoS ₂		78	62	[81]

determined from CV with a non-Faradaic current response. Then, the current density (j) is measured in the above potential range at multiple scan rates of 10–50 mV s⁻¹ (see Figs. S5–S7). Note that j can be expressed by $j = \nu C_{DL}$, where ν and C_{DL} denote the scan rate and electrochemical double-layer capacitance, respectively. Therefore, a j - ν plot yields a straight line, where the slope is equal to C_{DL} [65]. The C_{dl} value of (CoMo)S₂/RGO is 11.4 mF cm⁻², much higher than those of (CoMo)S₂ (8.9 mF cm⁻²) and bulk MoS₂ (0.7 mF cm⁻²), as shown in Fig. 5d. Moreover, the C_{DL} is also calculated by the EIS measurements. The corresponding C_{DL} values of (CoMo)S₂/RGO, (CoMo)S₂ and bulk MoS₂ are 10.2, 7.7, and 0.5 mF cm⁻², respectively, which are close to the corresponding C_{DL} values (11.4, 8.9, and 0.7 mF cm⁻²) determined by CV. This indicates that (CoMo)S₂/RGO possesses the most active sites through alloying with Co and compositing with RGO, and thus endows higher HER activity than those of bulk MoS₂ and (CoMo)S₂.

Another significant criterion for an advanced electrocatalyst is excellent electrochemical stability. Fig. 5e plots the current-time curve of (CoMo)S₂/RGO at a potential of -0.08 V. The current density decreases slightly after a scanning period of 20000 s, which might due to the consumption of H⁺ or the accumulation of H₂ bubbles on the electrode surface [60,66]. The inset in Fig. 5e shows an SEM image of (CoMo)S₂/RGO after the 20000-s durability test. It is clear that the (CoMo)S₂/RGO hybrid maintained its original structure, indicating a superior cyclic stability. Moreover, we compared the LSV curves of (CoMo)S₂/RGO at the initial cycle and after 5000 cycles of CV scanning (see Fig. S8). There is a tiny decay of potential (8 mV) for HER on (CoMo)S₂/RGO catalyst after 5000 CV cycles, also demonstrating the superior durability of (CoMo)S₂/RGO.

To further substantiate the hydrogen generation efficiency of (CoMo)S₂/RGO, the actual H₂ production was measured by gas chromatography and the corresponding results are shown in Fig. 5f. The detected H₂ amount is consistent with the theoretical value, corresponding to a high Faradic efficiency of about 98%. This confirms high electrocatalytic efficiency of (CoMo)S₂/RGO as an HER electrode in producing high-purity H₂.

5. Conclusions

In conclusion, we have developed a facile synthetic strategy to directly grow nanostructured (CoMo)S₂ on RGO as a high efficiency electrocatalyst for HER. The incorporated non-noble Co atoms in (CoMo)S₂ nanostructures not only form substantial desirable active sites, but also improve the electrical conductivity. The intrinsic activity and electrical conductivity are further enhanced by compositing with RGO. The optimized (CoMo)S₂/RGO hybrid exhibits excellent HER catalytic performance, outperforming most of reported MoS₂-based electrocatalysts. Both theoretical and experimental results in this work indicate that the (CoMo)S₂/RGO composite is a promising HER catalyst with high activity, low price and superior long-term stability.

Declaration of competing interest

The authors declare that they have no known competing financial interests or personal relationships that could have appeared to influence the work reported in this paper.

Acknowledgements

This project is financially supported by National Natural Science Foundation of China (Nos. 51671092 and 51631004), Program for JLU Science and Technology Innovative Research Team (No. 2017TD-09) and the Fundamental Research Funds for the Central Universities.

Appendix A. Supplementary data

Supplementary material related to this article can be found, in the online version, at doi:<https://doi.org/10.1016/j.apcatb.2019.118012>.

References

- [1] Q. Lu, Y. Yu, Q. Ma, B. Chen, H. Zhang, 2D transition-metal-dichalcogenide-nanosheet-based composites for photocatalytic and electrocatalytic hydrogen evolution reactions, *Adv. Mater.* 28 (2016) 1917–1933.
- [2] U. Gupte, C.N.R. Rao, Hydrogen generation by water splitting using MoS₂ and other transition metal dichalcogenides, *Nano Energy* 41 (2017) 49–65.
- [3] I. Staffell, D. Scamman, A.V. Abad, P. Balcombe, P.E. Dodds, P. Ekins, N. Shah, K.R. Ward, The role of hydrogen and fuel cells in the global energy system, *Energy Environ. Sci.* 12 (2019) 463–491.
- [4] J. Zhang, T. Wang, P. Liu, Z. Liao, S. Liu, X. Zhuang, M. Chen, E. Zschech, X. Feng, Efficient hydrogen production on MoNi₄ electrocatalysts with fast water dissociation kinetics, *Nat. Commun.* 8 (2017) 15437.
- [5] M.P. Suryawanshi, U.V. Ghorpade, S.W. Shin, U.P. Suryawanshi, E. Jo, J.H. Kim, Hierarchically coupled Ni:FeOOH nanosheets on 3D N-doped graphite foam as self-supported electrocatalysts for efficient and durable water oxidation, *ACS Catal.* 9 (2019) 5025–5034.
- [6] Y. Ouyang, C. Ling, Q. Chen, Z. Wang, L. Shi, J. Wang, Activating inert basal planes of MoS₂ for hydrogen evolution reaction through the formation of different intrinsic defects, *Chem. Mater.* 28 (2016) 4390–4396.
- [7] J. Zhang, T. Wang, P. Liu, S. Liu, R. Dong, X. Zhuang, M. Chen, X. Feng, Engineering water dissociation sites in MoS₂ nanosheets for accelerated electrocatalytic hydrogen production, *Energy Environ. Sci.* 9 (2016) 2789–2793.
- [8] P. Chen, T. Zhou, M. Zhang, Y. Tong, C. Zhong, N. Zhang, L. Zhang, C. Wu, Y. Xie, 3D nitrogen-anion-decorated nickel sulfides for highly efficient overall water splitting, *Adv. Mater.* 29 (2017) 1701584.
- [9] Y. Kim, D.H.K. Jackson, D. Lee, M. Choi, T.W. Kim, S.Y. Jeong, H.J. Chae, H.W. Kim, N. Park, H. Chang, T.F. Kuech, H.J. Kim, In situ electrochemical activation of atomic layer deposition coated MoS₂ basal planes for efficient hydrogen evolution reaction, *Adv. Funct. Mater.* 27 (2017) 1701825.
- [10] H.B. Wu, B.Y. Xia, L. Yu, X.Y. Yu, X.W. Lou, Porous molybdenum carbide nano-octahedrons synthesized via confined carburization in metal-organic frameworks for efficient hydrogen production, *Nat. Commun.* 6 (2015) 6512.
- [11] J.S. Li, Y. Wang, C.H. Liu, S.L. Li, Y.G. Wang, L.Z. Dong, Z.H. Dai, Y.F. Li, Y.Q. Lan, Coupled molybdenum carbide and reduced graphene oxide electrocatalysts for efficient hydrogen evolution, *Nat. Commun.* 7 (2016) 11204.
- [12] W.F. Chen, S. Iyer, S. Iyer, K. Sasaki, C.H. Wang, Y.M. Zhu, J.T. Muckerman, E. Fujita, Biomass-derived electrocatalytic composites for hydrogen evolution, *Energy Environ. Sci.* 6 (2013) 1818–1826.
- [13] J. Duan, S. Chen, B.A. Chambers, G.G. Andersson, S.Z. Qiao, 3D WS₂ nanolayers@ heteroatom-doped graphene films as hydrogen evolution catalyst electrodes, *Adv. Mater.* 27 (2015) 4234–4241.
- [14] X. Cao, C. Tan, X. Zhang, W. Zhao, H. Zhang, Solution-processed two-dimensional

- metal dichalcogenide-based nanomaterials for energy storage and conversion, *Adv. Mater.* 28 (2016) 6167–6196.
- [15] M. Chatti, T. Gengenbach, R. King, L. Spiccia, A.N. Simonov, Vertically aligned interlayer expanded MoS₂ nanosheets on a carbon support for hydrogen evolution electrocatalysis, *Chem. Mater.* 29 (2017) 3092–3099.
- [16] J. Deng, H. Li, J. Xiao, Y. Tu, D. Deng, H. Yang, H. Tian, J. Li, P. Ren, X. Bao, Triggering the electrocatalytic hydrogen evolution activity of the inert two-dimensional MoS₂ surface via single-atom metal doping, *Energy Environ. Sci.* 8 (2015) 1594–1601.
- [17] C. Tan, X. Cao, X.J. Wu, Q. He, J. Yang, X. Zhang, J. Chen, W. Zhao, S. Han, G.H. Nam, M. Sindoro, H. Zhang, Recent advances in ultrathin two-dimensional nanomaterials, *Chem. Rev.* 117 (2017) 6225–6331.
- [18] X.Y. Yu, Y. Feng, Y. Jeon, B. Guan, X.W. Lou, U. Paik, Formation of Ni-Co-MoS₂ nanoboxes with enhanced electrocatalytic activity for hydrogen evolution, *Adv. Mater.* 28 (2016) 9006–9011.
- [19] G. Zhang, H. Liu, J. Qu, J. Li, Two-dimensional layered MoS₂: rational design, properties and electrochemical applications, *Energy Environ. Sci.* 9 (2016) 1190–1209.
- [20] T.D. Thanh, N.D. Chuong, H.V. Hien, T. Kshetri, L.H. Tuan, N.H. Kim, J.H. Lee, Recent advances in two-dimensional transition metal dichalcogenides-graphene heterostructured materials for electrochemical applications, *Prog. Mater. Sci.* 96 (2018) 51–85.
- [21] D. Voiry, J. Yang, M. Chhowalla, Recent strategies for improving the catalytic activity of 2D TMD nanosheets toward the hydrogen evolution reaction, *Adv. Mater.* 28 (2016) 6197–6206.
- [22] Y. Guo, T. Park, J.W. Yi, J. Henzie, J. Kim, Z. Wang, B. Jiang, Y. Bando, Y. Sugahara, J. Tang, Y. Yamauchi, Nanoarchitectonics for transition-metal-sulfide based electrocatalysts for water splitting, *Adv. Mater.* 31 (2019) 1807134.
- [23] T.F. Jaramillo, K.P. Jørgensen, J. Bonde, J.H. Nielsen, S. Hørch, I. Chorkendorff, Identification of active edge sites for electrochemical H₂ evolution from MoS₂ nanocatalysts, *Science* 317 (2007) 100–102.
- [24] J. Deng, H. Li, S. Wang, D. Ding, M. Chen, C. Liu, Z. Tian, K.S. Novoselov, C. Ma, D. Deng, X. Bao, Multiscale structural and electronic control of molybdenum disulfide foam for highly efficient hydrogen production, *Nat. Commun.* 8 (2017) 14430.
- [25] L. Yu, B.Y. Xia, X. Wang, X.W. Lou, General formation of M-MoS₃ (M = Co, Ni) hollow structures with enhanced electrocatalytic activity for hydrogen evolution, *Adv. Mater.* 28 (2016) 92–97.
- [26] Z.W. Seh, J. Kibsgaard, C.F. Dickens, I. Chorkendorff, J.K. Nørskov, T.F. Jaramillo, Combining theory and experiment in electrocatalysis: insights into materials design, *Science* 355 (2017) eaad4998.
- [27] J. Kibsgaard, Z. Chen, B.N. Reinecke, T.F. Jaramillo, Engineering the surface structure of MoS₂ to preferentially expose active edge sites for electrocatalysis, *Nat. Mater.* 11 (2012) 963–969.
- [28] G. Ye, Y. Gong, J. Lin, B. Li, Y. He, S.T. Pantelides, W. Zhou, R. Vajtai, P.M. Ajayan, Defects engineered monolayer MoS₂ for improved hydrogen evolution reaction, *Nano Lett.* 16 (2016) 1097–1103.
- [29] Y. Yang, H. Fei, G. Ruan, C. Xiang, J.M. Tour, Edge-oriented MoS₂ nanoporous films as flexible electrodes for hydrogen evolution reactions and supercapacitor devices, *Adv. Mater.* 26 (2014) 8163–8168.
- [30] H. Li, C. Tsai, A.L. Koh, L. Cai, A.W. Contryman, A.H. Fragapane, J. Zhao, H.S. Han, H.C. Manoharan, F. Abild-Pedersen, J.K. Nørskov, X. Zheng, Activating and optimizing MoS₂ basal planes for hydrogen evolution through the formation of strained sulphur vacancies, *Nat. Mater.* 15 (2016) 48–53.
- [31] J. Xie, H. Zhang, S. Li, R. Wang, X. Sun, M. Zhou, J. Zhou, X. Lou, Y. Xie, Defect-rich MoS₂ ultrathin nanosheets with additional active edge sites for enhanced electrocatalytic hydrogen evolution, *Adv. Mater.* 25 (2013) 5807–5813.
- [32] J. Pető, T. Ollár, P. Vancsó, Z.I. Popov, G.Z. Magda, G. Dobrik, C. Hwang, P.B. Sorokin, L. Tapasztó, Spontaneous doping of the basal plane of MoS₂ single layers through oxygen substitution under ambient conditions, *Nat. Chem.* 10 (2018) 1246–1251.
- [33] X. Dai, K. Du, Z. Li, M. Liu, Y. Ma, H. Sun, X. Zhang, Y. Yang, Co-doped MoS₂ nanosheets with the dominant CoMoS phase coated on carbon as an excellent electrocatalyst for hydrogen evolution, *ACS Appl. Mater. Interfaces* 7 (2015) 27242–27253.
- [34] Q. Xiong, Y. Wang, P.F. Liu, L.R. Zheng, G. Wang, H.G. Yang, P.K. Wong, H. Zhang, H. Zhao, Cobalt covalent doping in MoS₂ to induce bifunctionality of overall water splitting, *Adv. Mater.* 30 (2018) 1801450.
- [35] L.X. Chen, Z.W. Chen, Y. Wang, C.C. Yang, Q. Jiang, Design of dual-modified MoS₂ with nanoporous Ni and graphene as efficient catalysts for the hydrogen evolution reaction, *ACS Catal.* 8 (2018) 8107–8114.
- [36] B. Delley, From molecules to solids with the DMol³ approach, *J. Chem. Phys.* 113 (2000) 7756–7764.
- [37] B. Delley, An all-electron numerical method for solving the local density functional for polyatomic molecules, *J. Chem. Phys.* 92 (1990) 508–517.
- [38] J.P. Perdew, K. Burke, M. Ernzerhof, Generalized gradient approximation made simple, *Phys. Rev. Lett.* 77 (1996) 3865–3868.
- [39] B. Delley, Hardness conserving semilocal pseudopotentials, *Phys. Rev. B* 66 (2002) 155125.
- [40] J.K. Nørskov, T. Bligaard, A. Logadottir, J.R. Kitchin, J.G. Chen, S. Pandalov, U. Stimming, Trends in the exchange current for hydrogen evolution, *J. Electrochem. Soc.* 152 (2005) J23–J26.
- [41] M.A. Lukowski, A.S. Daniel, F. Meng, A. Forticaux, L. Li, S. Jin, Enhanced hydrogen evolution catalysis from chemically exfoliated metallic MoS₂ nanosheets, *J. Am. Chem. Soc.* 135 (2013) 10274–10277.
- [42] X. Xie, Z. Ao, D. Su, J. Zhang, G. Wang, MoS₂/graphene composite anodes with enhanced performance for sodium-ion batteries: the role of the two-dimensional heterointerface, *Adv. Funct. Mater.* 25 (2015) 1393–1403.
- [43] X. Zou, Y. Zhang, Noble metal-free hydrogen evolution catalysts for water splitting, *Chem. Soc. Rev.* 44 (2015) 5148–5180.
- [44] D.C. Marcano, D.V. Kosynkin, J.M. Berlin, A. Sinitskii, Z. Sun, A. Slesarev, L.B. Alemany, W. Lu, J.M. Tour, Improved synthesis of graphene oxide, *ACS Nano* 4 (2010) 4806–4814.
- [45] M.M. Li, C.C. Yang, L.X. Chen, Q. Jiang, Hydrogen storage alloys/reduced graphite oxide: an efficient hybrid electrode with enhanced high-rate dischargeability, *Electrochim. Acta* 200 (2016) 59–65.
- [46] A. Kusoglu, A.Z. Weber, New insights into perfluorinated sulfonic-acid ionomers, *Chem. Rev.* 117 (2017) 987–1104.
- [47] X. Wei, G. Yin, J. Zhang, Rotating Electrode Methods and Oxygen Reduction Electrocatalysts, Elsevier, 2014, pp. 175–176.
- [48] X. Zhang, P. Ding, Y. Sun, X. Li, H. Li, J. Guo, CoMoS_{3.13} nanosheets grafted on B, N co-doped graphene nanotubes as bifunctional catalyst for efficient water electrolysis, *J. Alloy Compd.* 731 (2018) 403–410.
- [49] X. Geng, W. Wu, N. Li, W. Sun, J. Armstrong, A. Al-hilo, M. Brozak, J. Cui, T. Chen, Three-dimensional structures of MoS₂ nanosheets with ultrahigh hydrogen evolution reaction in water reduction, *Adv. Funct. Mater.* 24 (2014) 6123–6129.
- [50] J.V. Lauritsen, F. Besenbacher, Atom-resolved scanning tunneling microscopy investigations of molecular adsorption on MoS₂ and CoMoS hydrodesulfurization catalysts, *J. Catal.* 328 (2015) 49–58.
- [51] L. Ma, Y. Hu, G. Zhu, R. Chen, T. Chen, H. Lv, Y. Wang, J. Liang, H. Liu, C. Yan, Z. Tie, Z. Jin, J. Liu, In-situ thermal synthesis of inlaid ultrathin MoS₂/graphene nanosheets as electrocatalysts for the hydrogen evolution reaction, *Chem. Mater.* 28 (2016) 5733–5742.
- [52] M.S. Dresselhaus, A. Jorio, M. Hofmann, G. Dresselhaus, R. Saito, Perspectives on carbon nanotubes and graphene raman spectroscopy, *Nano Lett.* 10 (2010) 751–758.
- [53] H. Huang, J. Huang, W. Liu, Y. Fang, Y. Liu, Ultradispersed and single-layered MoS₂ nanoflakes strongly coupled with graphene: an optimized structure with high kinetics for the hydrogen evolution reaction, *ACS Appl. Mater. Interfaces* 9 (2017) 39380–39390.
- [54] P.J. Sheridan, Determination of experimental and theoretical k_{AS} factors for a 200-kV analytical electron microscope, *J. Electr. Microsc. Tech.* 11 (1989) 41–61.
- [55] G. Kothleitner, M.J. Neish, N.R. Lugg, S.D. Findlay, W. Grogger, F. Hofer, L.J. Allen, Quantitative elemental mapping at atomic resolution using X-ray spectroscopy, *Phys. Rev. Lett.* 112 (2014) 085501.
- [56] Y. Yan, X. Ge, Z. Liu, J.Y. Wang, J.M. Lee, X. Wang, Facile synthesis of low crystalline MoS₂ nanosheet-coated CNTs for enhanced hydrogen evolution reaction, *Nanoscale* 5 (2013) 7768–7771.
- [57] T.W. Lin, C.J. Liu, J.Y. Lin, Facile synthesis of MoS₂/carbon nanotube nanocomposite with high catalytic activity toward hydrogen evolution reaction, *Appl. Catal. B: Environ.* 134 (2013) 75–82.
- [58] X. Dai, K. Du, Z. Li, H. Sun, Y. Yang, W. Zhang, X. Zhang, Enhanced hydrogen evolution reaction on few-layer MoS₂ nanosheets-coated functionalized carbon nanotubes, *Int. J. Hydrog. Energy* 40 (2015) 8877–8888.
- [59] L. Ma, X. Zhou, X. Xu, L. Xu, L. Zhang, W. Chen, One-step hydrothermal synthesis of few-layered and edge-abundant MoS₂/C nanocomposites with enhanced electrocatalytic performance for hydrogen evolution reaction, *Adv. Powder Technol.* 26 (2015) 1273–1280.
- [60] K. Qi, S. Yu, Q. Wang, W. Zhang, J. Fan, W. Zheng, X. Cui, Decoration of the inert basal plane of defect-rich MoS₂ with Pd atoms for achieving Pt-similar HER activity, *J. Mater. Chem. A* 4 (2016) 4025–4031.
- [61] S. Stankovich, D.A. Dikin, R.D. Piner, K.A. Kohlhaas, A. Kleinhammes, Y. Jia, Y. Wu, S.T. Nguyen, R.S. Ruoff, Synthesis of graphene-based nanosheets via chemical reduction of exfoliated graphite oxide, *Carbon* 45 (2007) 1558–1565.
- [62] T.K.T. Ninh, D. Laurenti, E. Leclerc, M. Vrinat, Support effect for CoMoS and CoNiMoS hydrodesulfurization catalysts prepared by controlled method, *Appl. Catal. A* 487 (2014) 210–218.
- [63] M.R. Gao, M.K.Y. Chan, Y. Sun, Edge-terminated molybdenum disulfide with a 9.4-Å interlayer spacing for electrochemical hydrogen production, *Nat. Commun.* 6 (2015) 7493.
- [64] H.W. Liang, S. Bruller, R. Dong, J. Zhang, X. Feng, K. Mullen, Molecular metal-N_x centres in porous carbon for electrocatalytic hydrogen evolution, *Nat. Commun.* 6 (2015) 7992.
- [65] C.C.L. Mccrory, S. Jung, J.C. Peters, T.F. Jaramillo, Benchmarking heterogeneous electrocatalysts for the oxygen evolution reaction, *J. Am. Chem. Soc.* 135 (2013) 16977–16987.
- [66] J. Xie, J. Zhang, S. Li, F. Grote, X. Zhang, H. Zhang, R. Wang, Y. Lei, B. Pan, Y. Xie, Controllable disorder engineering in oxygen-incorporated MoS₂ ultrathin nanosheets for efficient hydrogen evolution, *J. Am. Chem. Soc.* 135 (2013) 17881–17888.
- [67] X. Wu, Z. Wang, M. Yu, L. Xiu, J. Qiu, Stabilizing the MXenes by carbon nanoplatelets for developing hierarchical nanohybrids with efficient lithium storage and hydrogen evolution capability, *Adv. Mater.* 29 (2017) 1607017.
- [68] L. Yang, W. Zhou, D. Hou, K. Zhou, G. Li, Z. Tang, L. Li, S. Chen, Porous metallic MoS₂-supported MoS₂ nanosheets for enhanced electrocatalytic activity in the hydrogen evolution reaction, *Nanoscale* 7 (2015) 5203–5208.
- [69] B.K. Barman, D. Das, K.K. Nanda, Facile and one-step synthesis of a free-standing 3D MoS₂-rGO/Mo binder-free electrode for efficient hydrogen evolution reaction, *J. Mater. Chem. A* 5 (2017) 18081–18087.
- [70] E. Ahn, B.S. Kim, Multidimensional thin film hybrid electrodes with MoS₂ multilayer for electrocatalytic hydrogen evolution reaction, *ACS Appl. Mater. Interfaces* 9 (2017) 8688–8695.

- [71] Z. Liu, Z. Gao, Y. Liu, M. Xia, R. Wang, N. Li, Heterogeneous nanostructure based on 1T-phase MoS₂ for enhanced electrocatalytic hydrogen evolution, *ACS Appl. Mater. Interfaces* 9 (2017) 25291–25297.
- [72] H. Yu, Y. Xue, L. Hui, C. Zhang, Y. Zhao, Z. Li, Y. Li, Controlled growth of MoS₂ nanosheets on 2D N-doped graphdiyne nanolayers for highly associated effects on water reduction, *Adv. Funct. Mater.* 28 (2018) 1707564.
- [73] R. Ye, P. Angel-Vicente, Y. Liu, M. Josefina Arellano-Jimenez, Z. Peng, T. Wang, Y. Li, B.I. Yakobson, S.H. Wei, M.J. Yacaman, J.M. Tour, High-performance hydrogen evolution from MoS_{2(1-x)}P_x solid solution, *Adv. Mater.* 28 (2016) 1427–1432.
- [74] D.J. Li, U.N. Maiti, J. Lim, D.S. Choi, W.J. Lee, Y. Oh, G.Y. Lee, S.O. Kim, Molybdenum sulfide/N-doped CNT forest hybrid catalysts for high-performance hydrogen evolution reaction, *Nano Lett.* 14 (2014) 1228–1233.
- [75] Y. Wang, S. Liu, X. Hao, J. Zhou, D. Song, D. Wang, L. Hou, F. Gao, Fluorine- and nitrogen-codoped MoS₂ with a catalytically active basal plane, *ACS Appl. Mater. Interfaces* 9 (2017) 27715–27719.
- [76] P. Kuang, T. Tong, K. Fan, J. Yu, In situ fabrication of Ni-Mo bimetal sulfide hybrid as an efficient electrocatalyst for hydrogen evolution over a wide pH range, *ACS Catal.* 7 (2017) 6179–6187.
- [77] Z. Wu, J. Wang, K. Xia, W. Lei, X. Liu, D. Wang, MoS₂-MoP heterostructured nanosheets on polymer-derived carbon as an electrocatalyst for hydrogen evolution reaction, *J. Mater. Chem. A* 6 (2018) 616–622.
- [78] Y. Shi, Y. Zhou, D.R. Yang, W.X. Xu, C. Wang, F.B. Wang, J.J. Xu, X.H. Xia, H.Y. Chen, Energy level engineering of MoS₂ by transition-metal doping for accelerating hydrogen evolution reaction, *J. Am. Chem. Soc.* 139 (2017) 15479–15485.
- [79] J. Liu, Y. Liu, D. Xu, Y. Zhu, W. Peng, Y. Li, F. Zhang, X. Fan, Hierarchical “nanoroll” like MoS₂/Ti₃C₂T_x hybrid with high electrocatalytic hydrogen evolution activity, *Appl. Catal. B: Environ.* 241 (2019) 89–94.
- [80] J. Xiong, J. Li, J. Shi, X. Zhang, W. Cai, Z. Yang, Metallic 1T-MoS₂ nanosheets in-situ entrenched on N,P,S-codoped hierarchical carbon microflower as an efficient and robust electro-catalyst for hydrogen evolution, *Appl. Catal. B: Environ.* 243 (2019) 614–620.
- [81] Z. Luo, Y. Ouyang, H. Zhang, M. Xiao, J. Ge, Z. Jiang, J. Wang, D. Tang, X. Cao, C. Liu, W. Xing, Chemically activating MoS₂ via spontaneous atomic palladium interfacial doping towards efficient hydrogen evolution, *Nat. Commun.* 9 (2018) 2120.